Tracking CO_2 plume footprints in reservoir-caprock system by fibre optic strain sensing

Yi Zhang[1*], Ziqiu Xue[1], Hyuck Park[1], Jiquan Shi[2], Tamotsu Kiyama[1], Xinglin Lei[3] & Yunfeng Liang[4]

[1] *Research Institute of Innovative Technology for the Earth (RITE) , 9-2, Kizugawadai, Kizugawa-Shi, Kyoto, 619-0292 JAPAN*

[2] *Department of Earth Science and Engineering, Royal School of Mines, Imperial College London, London SW7 2BP, United Kingdom*

[3] *Geological Survey of Japan, National Institute of Advanced Industrial Science and Technology, AIST Central #7, Higashi 1-1-1, Tsukuba, Ibaraki 305-8567, Japan*

[4] *Center for Engineering, Research into Artifacts (RACE), The University of Tokyo, Kashiwa, Chiba 277-8568, Japan*

Underground fluid storage and utilization, e.g., geological storage of carbon dioxide (CO_2) and natural gas, require effective tools to monitor the vertical pressure, deformation, and saturation migrations, and verify the secure containment of the reservoir-caprock system. Here we demonstrate how to utilize the swelling strain signals attributed to the footprints of pressure build up and the adsorption of supercritical CO_2 in natural clay-rich rocks to track the displacement of supercritical CO_2/brine under typical conditions of CO_2 geological storage. Our study effectively captured the breakthrough of CO_2 plume from the analogue "reservoir" part to the "caprock" part using the distributed strain, measured by a high-resolution single-mode Rayleigh-scattering based optical fibre sensor. The magnitude of strain change induced by CO_2 adsorptions on the clay minerals is found to be significantly greater than that caused by pore pressure

changes alone. The findings suggest that the measured strain changes can not only reveal the in situ deformation state but also be a valid indicator for tracking the movement of CO_2 plume as it enters the clay-rich critical region in reservoir-caprock systems, and thus serves as an early warning to the potential occurrence of large deformations caused by high pressure build up.

Underground geological reservoir engineering, e.g., enhanced oil recovery by water or gas injections, geothermal exploitations, shale gas fracking, and natural gas and CO_2 storages, often involve fluid injections and/or extractions. During these operations, the in situ state of pressure in the porous space would be inevitably changed, leading to the mechanical deformations in geological formations due to the poroelastic mechanism—the coupling between the deformation of porous matrix and pore fluid flow under stress. The deformations may be significant to cause induced seismicity[1] and observable uplift or subsidence of earth ground[2]. CO_2 sequestration into underground geological reservoirs is now considered as one of the best near-term solutions to mitigate global warming effects[3–5]. In a large-scale geological CO_2 storage project, another potential problem is associated to the impact of pressure build up on the long-term integrity of a CO_2 repository[6] and the risk of CO_2 or brine leakages[7]. CO_2 could migrate into the caprock if the pressure in the reservoir overwhelms the threshold pressure of caprock. In addition, the reactivation of faults and breach of caprock could also create or enhance vertical leakage pathways, contributing to an unexpected leakage of CO_2[8,9]. For these reasons, valid methods are required to closely monitor the development of pressure build up, deformations and CO_2 plume migration in reservoir formations and caprocks above the storage reservoir.

Besides poroelastic changes, one of the poromechanical responses, i.e., clay swelling phenomena has been well studied from different aspects of geoscience, e.g., in shales, coals, soils, etc. CO_2 can be energetically adsorbed on the surface and edge of clay minerals or into the crystal interlays, resulting in significant swelling[10–12]. The swelling can be also significant to change the stress state[13]. At a given pressure, the swelling is more pronounced with carbon dioxide than with other fluids, like water and methane[12]. Therefore, it might be anticipated that, as CO_2 displaces brine through clay-rich strata (e.g., caprocks), strain changes due to the preferential adsorption of CO_2 in the clay, in addition to the poroelastic mechanism, could be observed. Taking advantage of this characteristic, we propose to monitor the migration of CO_2/brine displacement front in clay-rich region in a reservoir-caprock via monitoring the strain (Fig. 1 a).

With the recent development of distributed fibre optical strain sensing (DFOSS) technique[14], the response at each spatial location due to rock deformation may be tracked in real-time. Therefore, the tool can potentially give an improved understanding of the roles of pressure migration and CO_2 plume migration along the vertical direction while incorporating the concept of in-reservoir and above-zone pressure monitoring[15] (e.g., at Decatur CO_2 storage site[16]), and also give important constraints in geomechanical modelling[7,17].

This study aims to measure rock swelling strain caused by CO_2 displacing brine through an analogue reservoir-caprock system. A clay-rich Tako sandstone (from Gunma, Japan) developed with both coarse-grain high-permeability (“reservoir”) and fine-grain low-permeability (“caprock”) regions is used for the experiment (Fig. 1 b). The strain is continuously measured using a high-resolution DFOSS tool (see Methods) during CO_2 drainage and brine imbibition in the sample under a typical reservoir condition (10 MPa and 40 °C). In addition, the X-ray CT is used to image the spatial fluid saturation in the rock.

Experimental tests

The experiment was started from a dry state of the rock sample after two days of vacuum-drying. Then the sample was pressurized step-by-step by increasing the confining pressure (0~15 MPa). After this the confining pressure was reduced to 5 MPa and then the brine (potassium iodide solution, 11.5 wt%) was injected to the vacuumed sample until the sample was fully saturated. Continuous brine injection was conducted to measure the permeability. Then we elevated the confining pressure (to 15 MPa) and pore pressure (to 10 MPa) to investigate the poroelastic effect. After that the CO_2 drainage and brine imbibition were conducted. During the CO_2 drainage, the injection pressure at the inlet and outlet were initially set to 10.1 and 10 MPa, respectively. Under the low differential pressure, the CO_2 fluid flow front gradually migrated with the displacement at the coarse-grain part for approximately 40 hours and then it was blocked by one low-permeability capillary barrier in the fine-grain part. After we elevated the inlet pressure up to 10.3 MPa step-by-step (8 steps, approximately 1 hour/step), the CO_2 flow was able to percolate into the fine-grain part. The overall drainage persisted approximately 68 hours. After the drainage, a forced brine injection from the outlet with a pressure of approximately 10.8 MPa was conducted. The brine injection lasted approximately 20 hours. During these operations, the X-ray CT imaging was only conducted at the day time intermittently to obtain the information of spatial saturation of CO_2 in the rock sample. The distributed strain was continuously measured using the DFOSS system.

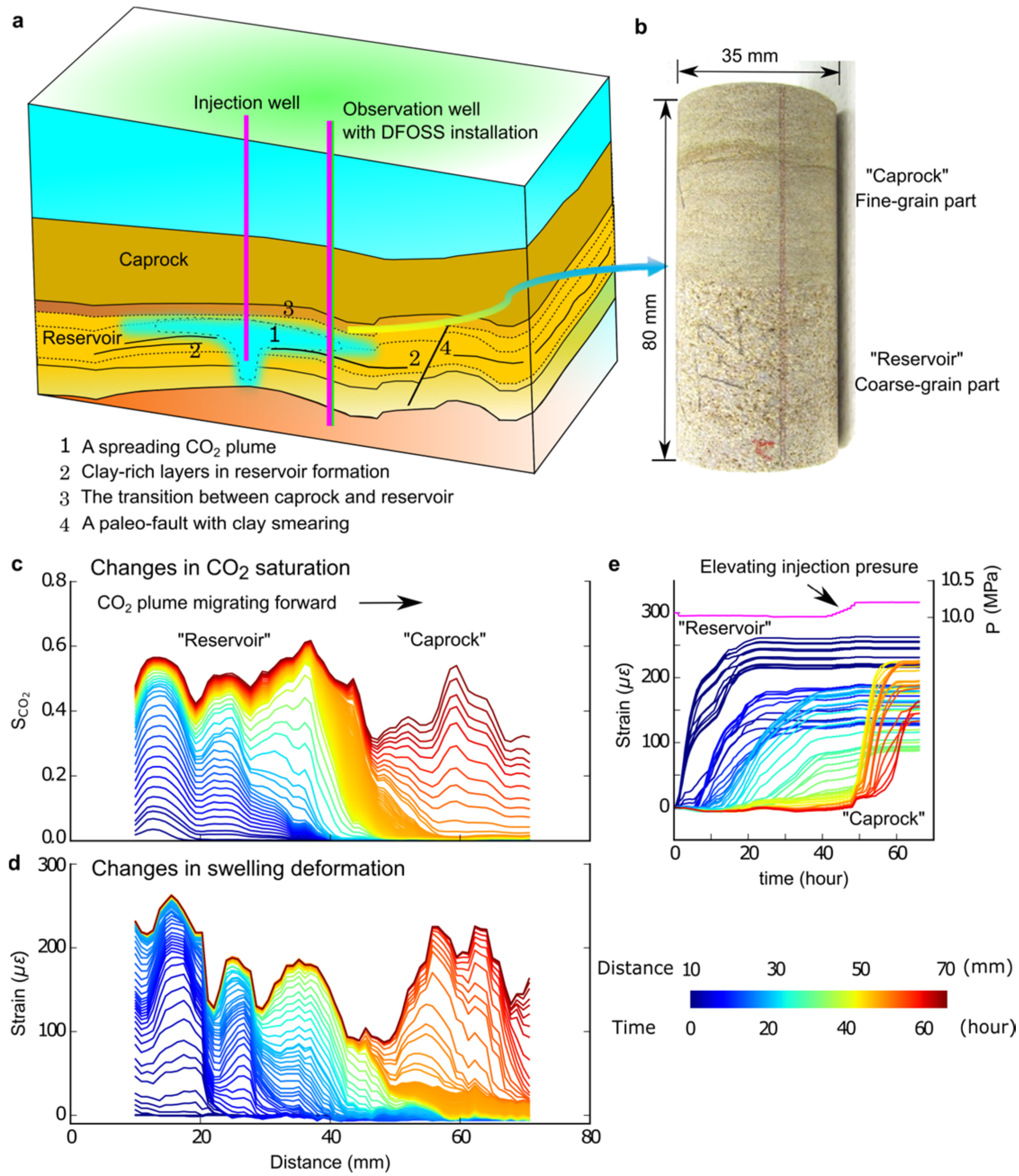

Fig.1 **a**, Schematic geological model of CO_2 storage site, with emphasis on the clay-rich components in the caprock-reservoir transition, tight clay-rich layers within reservoir formations, and paleo-fault with clay smearing. An observation well with the DFOSS installation is used to illustrate the distributed strain sensing across the overall system. **b**, The Tako sandstone sample—an analogue to the reservoir-caprock system or clay-rich layers. **c**, The experimentally obtained profiles of averaged CO_2 saturation (S_{CO2}) (computed from X-ray CT imaging) along the rock sample. Note that the displayed saturation data are linearly interpolated and coloured with elapse time for a better view. The only measured data is shown in the Supplementary Fig.7. **d**, The profiles of circumferential strain (experimentally measured using the DFOSS) on the surface of the rock sample. **e**, The circumferential strain against time coloured with spatial distance to the inlet end of the sample. Note that the pressure increase between 40 and 50 hours cause only slight swelling strains (< 10 $\mu\epsilon$).

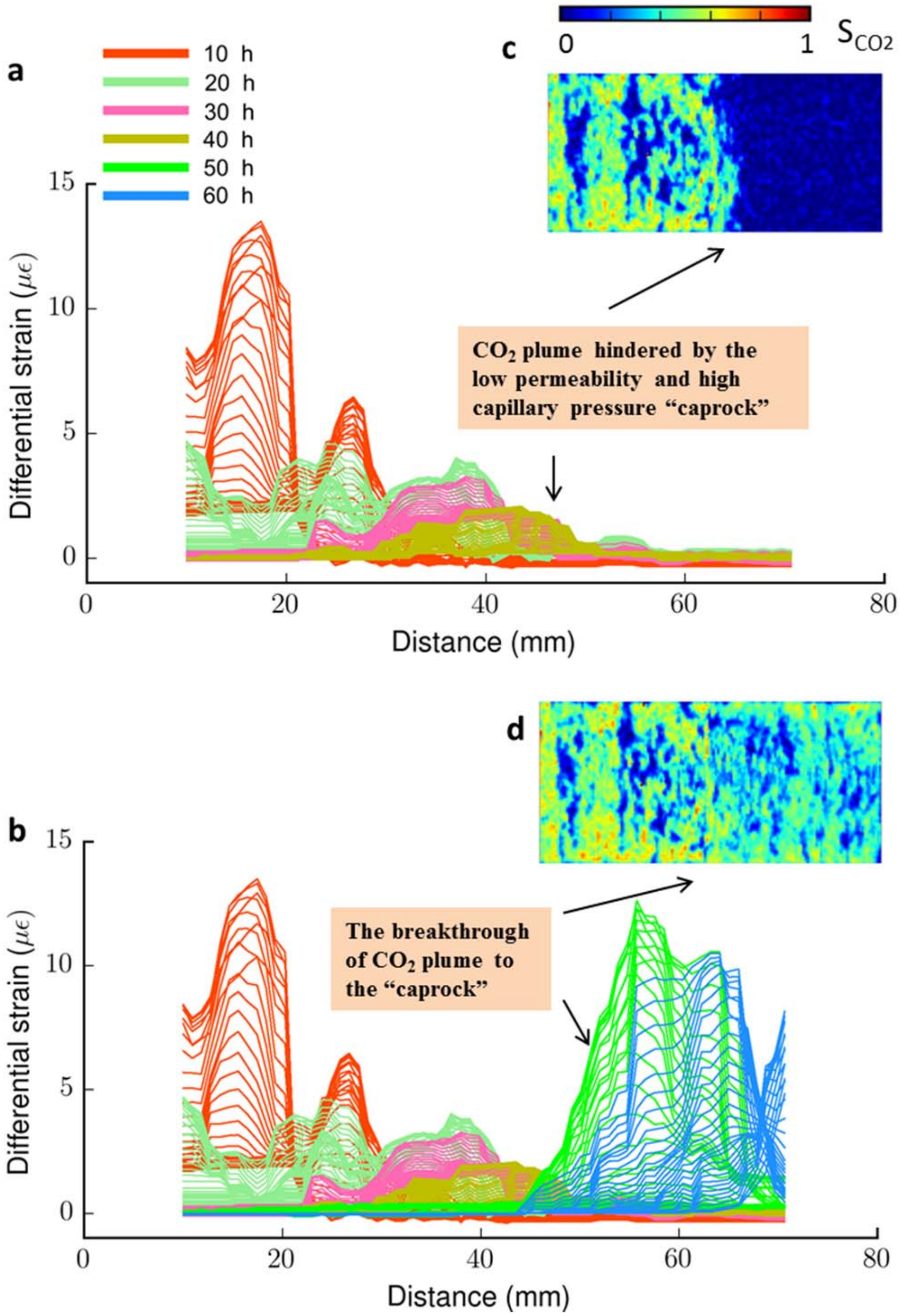

Fig.2 Differential strain changes (strain/hour) calculated by subtracting two sets of measured strains with a time interval of approximately 3.3 hours. Overall results are divided in to six stages (with a time interval of approximately 10 hours) that expressed

in different colours to emphasize the temporary changes. **a**, Changes before stage 5 (former 40 hours); **b**, Changes of all stages. Colours in **a** and **b** denote time. **c**/**d**, Images of CO_2 saturation (S_{CO2}) at 40/60 hours are attached. The changes clearly show the structure-affected deformation behaviour and the breakthrough of CO_2 plume from the high permeability (“reservoir”) part to the low permeability (“caprock”) part.

CO_2 plume migration and distributed strain response

The experimental results reveal that the deformation in the reservoir-caprock system can be effectively monitored using the DFOSS tool. The strain changes well correspond to the spreading of CO_2 plume and show significant differences between the reservoir and caprock parts. During the CO_2 drainage (Fig. 1c-e), the injected CO_2 displaced the brine out from the rock sample as indicated by the saturation changes. The CO_2 plume was retarded by the low-permeability caprock part and then migrated through it after elevating the injection pressure. Before the breakthrough of CO_2 plume to the caprock part, the corresponding strain mainly responded at the reservoir region with the gradually increased strain magnitude (0~260 με). Unlike the relatively steep gradients near the CO_2 saturation front, the changes of strain showed a more gradual trend and occurred earlier than the changes in the CO_2 saturation due to the mechanical effect and forward pressure migration. However, the large changes (~200 με) were mainly within the reservoir part where the CO_2 plume developed. Moreover, the strain changes show spatial dependence on the rock structure. Several local low-porosity layers showed strain changes with a reduced magnitude and also a lower CO_2 saturation. These layers acted as the temporal in-passing capillary barriers for the forward CO_2/brine displacement.

The breakthrough of CO_2 plume occurred after the injection pressure was step-elevated from 10.1 MPa to 10.3 MPa. Subsequently, significantly large and rapid strain changes in the caprock part were observed (Fig. 1d and e). The breakthrough pressure for CO_2 percolating through the rock was less than 300 kPa under the setting condition. The breakthrough behaviour was well indicated by the strain signals. Note that the pressure change (200 kPa) itself only produced a small strain (< 10 με) (Fig. 1e). The large strain changes in the caprock part mainly occurred following the migration of CO_2 plume with CO_2/brine replacement. The dynamic deformations are better depicted using the differential strain between steps, which show more discernible time-dependent behaviour (Fig. 2). Overall, during the drainage, the changes in strain can well reveal the migration of CO_2/brine displacement front in the reservoir and breakthrough to the caprock in the rock sample. On the contrary, during the imbibition, the rock sample showed a general trend of shrinking after an initial short period of swelling caused by the elevated pore pressure (Supplementary Fig. 8).

Adsorption-induced swelling as a CO_2 migration indicator

Note that the values of the strain changes are significantly larger than that would be expected due to pure pore pressure effects as estimated from the poroelastic mechanism. Under the fully brine saturated state, the bulk modulus of the rock was estimated approximately 7.6 ~ 8.8 GPa (the coarse-grain part) and 8.3 ~ 10.0 GPa (the fine-grain part, see Supplementary Fig. 9). Consequently, under the given maximum 300 kPa of change in the effective pressure, the upper limit of the poroelastic (circumferential) deformation was expected to be smaller than 20 $\mu\epsilon$. The limit well constraints the actually produced strain changes (< 10 $\mu\epsilon$) due to pressure change (200 kPa) alone when elevating the pore pressure during the drainage. However, the measured strain values (~260 $\mu\epsilon$) after CO_2 displacing brine are in fact much larger than this limit, and even larger than the strain value produced by 2 MPa of pore pressure changes (approximately 100 $\mu\epsilon$) when the sample is fully saturated with brine (Supplementary Fig. 9b).

The large changes in strain are likely related to the abundant content of clay mineral (kaolinite) in the rock. CO_2 is preferentially adsorbed on clay minerals with respect to brine. An injection of CO_2 into a clay-rich rock initially full of brine causes a differential swelling of the porous matrix. In contrast, during brine imbibition, the CO_2 desorption by brine induces a shrinkage. Several recent studies have shown that CO_2 can be adsorbed in clay-rich rocks accompanying significant swelling[10]. The CO_2

adsorption in kaolinite was supported by both physical chemistry studies[18–20] and direct experimental studies[12]. Unlike the very large swelling strain (~10^4 με) observed in coal samples due to CO_2 adsorption, however, the CO_2 adsorption induced strain in a kaolinite bearing rock (i.e. shales) can be as large as ~10^3 με[12]. Compared with other fluids, e.g., methane and water, the adsorption ability of CO_2 in clay minerals is more outstanding[12,21]. Such enhanced swellings can also be found in several previous studies where strain measured using conventional strain gauges when CO_2 displacing brine in rocks [22]. However, it lacks an explicit explanation in these studies.

We numerically simulated the effects of adsorption induced strain using a sequentially coupled one-dimensional two-phase fluid flow and poromechanical model. A Langmuir-type adsorption relationship with saturation scaling was used to model adsorption induced strain changes during CO_2 saturating[32]. In order to see the maximum value of probable deformations due to the poroelastic mechanism alone, with a comparison to the adsorption included model, we used a lower limit of measured bulk modulus (7.6 GPa). The modelling results show that the poroelastic alone can only produce a maximum circumferential strain of approximately 16 με (Supplementary Fig. 10). In contrast, by adding the adsorption induced deformation mechanism, the magnitude of measured strain (~260 με) can be well interpreted (Supplementary Fig. 11). Moreover, the modelling can generally reproduce the behaviour of the breakthrough to caprock and structure-dependent deformations. The rock porosity structure controls the spatial distribution of capillary entry pressure, which further causes differences in the spatial CO_2 saturation. The latter controls the adsorption induced deformations together with the role of pore pressure.

Implications for reservoir monitoring using DFOSS

Clay-rich rocks are common in a reservoir-caprock system for geological storage of CO_2 and natural gas. These rocks may appear at the transition between the reservoir and caprock, tight interbedding shale-contained layers within overall high-permeability reservoir (e.g. the CO_2 storage sites at Sleipner, Norway[23] and Nagaoka, Japan) and sealed paleo-fault zones with the clay smearing[24]. In a large-scale CO_2 storage project, during CO_2 injection and post-injection stages, the appearances and migrations of CO_2 and deformations at all these parts are critical and required to be closely monitored. In addition, even some of the targeted reservoir formations for CO_2 storage have been found to contain a rich amount of clay minerals. For example, the sampled rocks from the Takinoue formation, which is the targeted CO_2 storage reservoir for a large-scale CO_2 storage demonstration project at Tomakomai, Hokkaido, Japan, have been found containing smectite and montmorillonite[25]. Our studies indicate that the changes in strain can be significantly enhanced (in several hundreds of $\mu\epsilon$) with the adsorption of CO_2 in the clay-rich parts, under slight pore pressure changes, compared with the role of poroelastic effect played alone. Moreover, to field applications, utilizing these signals, one can directly monitor the migration of CO_2 plume—whether the CO_2 plume has passed through the monitored regions (e.g., lower caprocks), and diagnose the potential fluid leakage risk, to assist in further decision making, injection planning and reservoir management. The study helps in how to distinguish between the pore pressure propagation effects (pressure footprint) and CO_2 migration through caprock (saturation footprint) from the deformation pattern and magnitude. The former shows gradual changes with the magnitude increasing from small to large with the pressure build up; whereas the latter could give a relatively large strain change in a short term once CO_2 has migrated to the clay-rich caprock.

Our study straightforwardly demonstrates that the spatial strain can be effectively measured using the DFOSS with high accuracy and resolution. Overall, the utilization of DFOSS tool can not only directly give the information in deformation but also the migration of fluid plume in a reservoir-caprock system. The findings and application of distributed fibre-optical strain sensor are thought to be advantageous in underground reservoir monitoring and management. In practice, the technique can be integrated with other tools, e.g., pressure[16], seismic[33], electric, microseismic monitoring[9], etc., for further more solidly tracking CO_2 plume and diagnosing potential reservoir geomechanical and fluid flow problems in a broad area. Here we focus on the strain responses to CO_2 injections for the purpose of CO_2 storage in underground reservoirs. However, the same technique can be also valid for other geological problems involving geomechanical monitoring, e.g., fluid extractions or injections in oil and gas reservoirs[26] and geothermal exploitations, mine exploitations, crustal deformations relevant to earthquakes[27], etc.

End of main text

METHODS

Rock sample

The rock sample used in this study is cored along a direction perpendicular to the bedding plane from a low-permeability (~ 0.02 mD) heterogeneous Tako sandstone (from Gunma, Japan). The cylinder sample, with a diameter of 35 mm and length of 80 mm, visually contains two regions, a coarse-grain and a fine-grain region (Fig. 1 b). The two parts have different petrophysical characteristics, including permeability, porosity (Supplementary Fig. 1) and pore size (Supplementary Fig. 2). The coarse-grain part has a larger pore size, porosity and permeability than the fine-grain part. Both of the two parts have high content of the clay mineral—kaolinite (Supplementary Fig. 3). According to the results of X-ray powder diffraction (XRD) analysis, the mineral compositions of the two parts (coarse and fine) are as follows: quartz (52.2% and 38.0%), kaolinite (36.0% and 52.8%), Muscovite (2.8% and 8.3%), K-feldspar (8.0% and 0.9%) (Supplementary Fig. 4). The sample could be seen as an analogue for two typical components in a reservoir-caprock system, such as the transition part between caprock and reservoir, sand mud alternation, and the tight interbedding layers within a reservoir (Fig. 1 a). The rocks in these components are usually clay-rich and have a low permeability compared to common reservoir sandstones.

Experimental settings

A quartz-made single-mode holey optical fibre was spirally bonded on the surface of the cylindrical sample in order to increase the measurement density (Supplementary Fig. 5). The holey fibre, with empty holes distributed in the cladding outside fibre's glass core, has a low bending loss for light signals, making it is suitable to measure the circumferential deformation of cylindrical sample under high stress conditions. To be able to apply a high injection pressure and confining pressure, the sample was jacketed using the epoxy paste to insulate the confining oil and pore fluids and then put into a core holder (Supplementary Fig. 6), which is made of an X-ray transparent and high strength material (PEEK). Two high accuracy syringe pumps were connected to the two side of rock sample to control the pressure and injection. In order to keep the CO_2 in a supercritical condition, the pore pressure was set above 10 MPa and the temperature of the whole system was kept at 40 °C using the carbon cloth heaters or water circulation heaters. The fibre was passed through the being pressurized core holder by a feedthrough component, which prohibits the leakage of fluids. The entire core holder was put on the bed of a medical X-ray CT scanner to make imaging available. The fibre segment was connected to prolonged segments and then connected to an integrated measurement equipment (Neubrex 7020 type). The strain sensing tool is developed on the basis of a coherent optical time-domain reflectometer (COTDR) method utilizing Rayleigh backscattering signals from the inherent random defects in an intact fibre to detect deformations[28,29]. It can give a high measurement accuracy (0.5 με) and spatial resolution (2 cm), allowing to monitor very small strains in a long-range distributed mode. The accuracy of the DFOSS technique has been demonstrated in several prior tests with a comparison with the conventional strain gauges[30,31] and successfully applied in field wellbores with water injection tests and measurements[32].

Measurement principle of COTDR using optical fibre

The COTDR (coherent optical time domain reflectometry) technique calculates strain or temperature using the shift in the frequency of the power spectral of the Rayleigh backscatter traces from a single-mode fibre[28]. In the method, the light source is precisely frequency-controlled. The frequency shift is calculated using the cross-correlation between two spectral of COTDR measurements at two time points. At a spatial location of a fibre, if there is no change in strain and temperature during the time interval, the two power-spectral should be coincident in the frequency domain. Instead, a phase difference between them exists if there are changes in strain or temperature due to the changes in local refractive index. The strain or temperature is calculated from the shift in the frequency of the power spectral.

Model of adsorption induced swelling strain

The adsorption induced swelling strain ε in confine pores can be described by a refined poromechanical model[33],

$$\varepsilon = \varepsilon_0 + \int_{P_{b0}}^{P_b} \frac{dP_\mathrm{b}}{K}\{\alpha(1-\chi)^{-1} - 1\} \qquad (1)$$

where ε_0 is the initial strain, K is the bulk modulus, α is the Biot's coefficient, $\boldsymbol{P}_\mathbf{b}$ (**0** denotes the initial state) is the new defined effective pore pressure, and χ is the confinement degree. The confinement degree χ scales the pore fluid pressure $\boldsymbol{P}_\mathbf{f}$ and $\boldsymbol{P}_\mathbf{b}$ as

$$dP_\mathrm{f} = \frac{dP_\mathrm{b}}{1-\chi} \qquad (2)$$

The equation (1) predicts a swelling strain similar to the Langmuir type sorption model. Analytically, it is equivalent to an empirical Langmuir type deformation model[34],

$$\varepsilon_\mathrm{sorp} = \frac{\varepsilon_\mathrm{max} P}{P + P_\varepsilon} \qquad (3)$$

where $\varepsilon_\mathrm{sorp}$ is the adsorption induced volumetric strain at pressure P, and ε_max and P_ε are similar to the Langmuir-type constants for scaling the strain.

The poroelastic model for the two-phase fluid flow

A sequentially coupled one-dimensional two-phase fluid flow and poromechanical model was used for the numerical simulation. The model was developed on the basis of an open source reservoir simulator (MRST)[35].

The two-phase fluid flow equation is as following,

$$\frac{\phi\rho_\alpha S_\alpha}{\partial t} + \nabla\cdot(\rho_\alpha v_\alpha) = \rho_\alpha Q_\alpha \qquad (4)$$

where ϕ is the porosity, α (w or nw) denotes the wetting and nonwetting fluid, ρ and S are the density and saturation of the fluids, and $Q$is the source. The flow flux v is expressed using the extended Darcy's law,

$$v_\alpha = -\frac{Kk_{r\alpha}}{\mu_\alpha}(\nabla p_\alpha - \rho_\alpha g\nabla h) \qquad (5)$$

where *K* is the permeability, $k_{r\alpha}$ is the relative permeability, μ_α is the viscosity of a fluid, p is the pressure, and $\rho_\alpha g\nabla h$ accounts for the gravity force.

In the modelling, the permeability at each location is estimated using the Leverett J-function as following[36],

$$K_i = \phi_i \frac{1}{\overline{P_c}(S_w)^2}[\sigma\cos(\theta)J(S_{w,i})]^2 \qquad (6)$$

where *i* denotes the spatial location, σ and θ are the interfacial tension and contact angle between CO_2 and brine, and $\overline{P_c}$ is the global capillary pressure at each saturation (S_w) estimated from mercury injection method. The Leverett J-function J is expressed as

$$J(S_w) = \frac{P_c}{\sigma\cos\theta}\sqrt{\frac{k}{\phi}} \qquad (7)$$

The local capillary pressure is also accounted by scaling the global capillary pressure using local porosity ratio as following,

$$P_c(S_w, i) = \overline{P_c}(S_w, i)(\frac{\phi_0}{\phi})^n \qquad (8)$$

where ϕ_0 is the mean porosity and *n* is a tuning exponent.

The mechanical responses are modelled using following equations,

$$\nabla\cdot\sigma_{ij} + f = 0 \quad (9)$$

$$\varepsilon_{ij} = \frac{1}{2}(\nabla u_i + \nabla u_j) \quad (10)$$

$$\varepsilon_{ij} = \frac{1}{2G}\sigma_{ij} - (\frac{1}{6G} - \frac{1}{9K})\sigma_{kk}\delta_{ij} + \frac{b}{3K}p\delta_{ij} + \frac{\varepsilon_{\text{sorp}}}{3}\delta_{ij} \quad (11)$$

where σ_{ij} is the stress tensor, *f* is the body force, ε_{ij} is the strain tensor, u_i is the displacement, G and K are the shear and bulk modulus, b is the Biot's coefficient, p is the pore pressure, δ_{ij} is the Kronecker delta, and $\varepsilon_{\text{sorp}}$ is the adsorption-induced strain.

Calculation of CO_2 saturation from X-ray CT imaging

A medical X-ray CT scanner (Aquilion ONE TSX 301A, Toshiba Medical Systems Corp.) was utilized to image the rock sample. The reconstructed image volume has total 160 slices along the axis direction (80 mm long). Each slice has total 512×512 pixels. The length of each pixel is approximately 71µm.

The following equations is used to determine the CO_2 saturation, S_{CO_2}, of each voxel,

$$S_{\text{CO}_2} = c\left(CT_{\text{obs}} - CT_{\text{brine}}^{\text{sat}}\right) = \frac{CT_{\text{obs}} - CT_{\text{brine}}^{\text{sat}}}{CT_{\text{CO}_2}^{\text{sat}} - CT_{\text{brine}}^{\text{sat}}} \quad (12)$$

where $CT_{\text{brine}}^{\text{sat}}$ and $CT_{\text{CO}_2}^{\text{sat}}$ are the voxel CT values of the brine-saturated and CO_2 saturated states, respectively, CT_{obs} is the CT value of the state which saturation is being calculated, c is the coefficient that relates S_{CO_2} to the changes between CT values.

Mineral analysis

The mineral analysis was conducted using the Rigaku Smartlab Intelligent X-ray diffraction (XRD) system.

Acknowledgements

This work is part of an R&D project "the Development of Safety Management Technology for Large-Scale CO2 Geological Storage, commissioned to the Geological Carbon Dioxide Storage Technology Research Association by the Ministry of Economy, Trade and Industry (METI) of Japan". We thank K. Nakano for the help in XRD mineral analysis.

Author contributions

Z.X. and Y.Z. conceived the project, Y.Z. designed the experiments, H.P., Y.Z. and T.K. performed the experiments, Y.Z., J.S. and X.L. contributed to data analysis and theoretical interpretations, Y.L contributed to theoretical interpretations and molecular dynamics simulations, Y.Z wrote the first draft of the paper and all co-authors improved the final version.

Data availability

The authors declare that all necessary data supporting the findings of this study are available within the article and its Supplementary Information files. Any further data (for example, X-ray CT images and strains) are available from the corresponding author upon request.

1. Hincks, T., Aspinall, W., Cooke, R. & Gernon, T. Oklahoma's induced seismicity strongly linked to wastewater injection depth. *Science (80-.).* **7911,** 1–9 (2018).

2. Shirzaei, M., Ellsworth, W. L., Tiampo, K. F., González, P. J. & Manga, M. Surface uplift and time-dependent seismic hazard due to fluid injection in eastern Texas. *Science (80-.).* **353,** 1416–1419 (2016).

3. Benson, S. *et al.* Underground geological storage. *IPCC Spec. Rep. carbon dioxide capture storage* 195–276 (2005).

4. Bickle, M. J. Geological carbon storage. *Nat. Geosci.* **2,** 815–818 (2009).

5. Orr, F. M. Onshore geologic storage of CO_2. *Science (80-.).* **325,** 1656–1658 (2009).

6. Kampman, N. *et al.* Observational evidence confirms modelling of the long-term integrity of CO_2-reservoir caprocks. *Nat. Commun.* **7,** 12268 (2016).

7. Rutqvist, J. The geomechanics of CO_2 storage in deep sedimentary formations. *Geotech. Geol. Eng.* **30,** 525–551 (2012).

8. Zoback, M. D. & Gorelick, S. M. Earthquake triggering and large-scale geologic storage of carbon dioxide. *Proc. Natl. Acad. Sci. U. S. A.* **109,** 10164–8 (2012).

9. Verdon, J. P. *et al.* Comparison of geomechanical deformation induced by megatonne-scale CO_2 storage at Sleipner, Weyburn, and In Salah. *Proc. Natl. Acad. Sci. U. S. A.* **110,** E2762-71 (2013).

10. Busch, A. *et al.* On sorption and swelling of CO_2 in clays. *Geomech. Geophys. Geo-Energy Geo-Resources* **2,** 111–130 (2016).

11. Wan, J. *et al.* Supercritical CO_2 uptake by nonswelling phyllosilicates. *Proc. Natl. Acad. Sci.* (2018).

12. Heller, R. & Zoback, M. Adsorption of methane and carbon dioxide on gas shale and pure mineral samples. *J. Unconv. Oil Gas Resour.* **8,** 14–24 (2014).

13. Wentinck, H. M. & Busch, A. Modelling of CO2 diffusion and related poro-elastic effects in a smectite-rich cap rock above a reservoir used for CO2 storage. *Geol. Soc. London, Spec. Publ.* **454,** 155–173 (2017).

14. Masoudi, A. & Newson, T. Contributed Review: Distributed optical fibre dynamic strain sensing. *Rev. Sci. Instrum.* **87,** 11501 (2016).

15. Cameron, D. A., Durlofsky, L. J. & Benson, S. M. Use of above-zone pressure data to locate and quantify leaks during carbon storage operations. *Int. J. Greenh. Gas Control* **52,** 32–43 (2016).

16. Strandli, C. W. & Benson, S. M. Identifying diagnostics for reservoir structure and CO2 plume migration from multilevel pressure measurements. *Water Resour. Res.* **49,** 3462–3475 (2013).

17. Shi, J.-Q., Sinayuc, C., Durucan, S. & Korre, A. Assessment of carbon dioxide plume behaviour within the storage reservoir and the lower caprock around the KB-502 injection well at In Salah. *Int. J. Greenh. Gas Control* **7,** 115–126 (2012).

18. Busch, A. *et al.* Carbon dioxide storage potential of shales. *Int. J. Greenh. Gas Control* **2,** 297–308 (2008).

19. Chen, Y.-H. & Lu, D.-L. CO2 capture by kaolinite and its adsorption mechanism. *Appl. Clay Sci.* **104,** 221–228 (2015).

20. Jedli, H., Jbara, A., Hedfi, H., Bouzgarrou, S. & Slimi, K. Carbon dioxide adsorption isotherm study on various cap rocks in a batch reactor for CO2 sequestration processes. *Appl. Clay Sci.* **136,** 199–207 (2017).

21. Brochard, L., Vandamme, M., Pellenq, R. J.-M. & Fen-Chong, T. Adsorption-induced deformation of microporous materials: coal swelling induced by CO2–CH4 competitive adsorption. *Langmuir* **28,** 2659–2670 (2012).

22. Xue, Z. & Ohsumi, T. Seismic wave monitoring of CO2 migration in water-saturated porous sandstone. *Explor. Geophys.* **35,** 25–32 (2004).

23. Arts, R., Chadwick, A., Eiken, O., Thibeau, S. & Nooner, S. Ten years' experience of monitoring CO2 injection in the Utsira Sand at Sleipner offshore Norway. *First Break* **26,** 65–72 (2008).

24. Vrolijk, P. J., Urai, J. L. & Kettermann, M. Clay smear: Review of mechanisms and applications. *J. Struct. Geol.* **86,** 95–152 (2016).

25. Okubo, S., Takahashi, K. & Nakashima, H. The relationship between the expandability of clay mineral and the permeability of Takinoue pyroclastic layer 'T1 member' in Yufutsu Oil and Gas Field, Hokkaido, Japan. *J. Japanese Assoc. Pet. Technol.* **76,** 209–218 (2011).

26. Guglielmi, Y., Cappa, F., Avouac, J.-P., Henry, P. & Elsworth, D. Seismicity triggered by fluid injection–induced aseismic slip. *Science (80-.).* **348,** 1224–1226 (2015).

27. Wang, K., Hu, Y. & He, J. Deformation cycles of subduction earthquakes in a viscoelastic Earth. *Nature* **484,** 327–332 (2012).

28. Koyamada, Y., Imahama, M., Kubota, K. & Hogari, K. Fiber-optic distributed strain and temperature sensing with very high measurand resolution over long range using coherent OTDR. *J. Light. Technol.* **27,** 1142–1146 (2009).

29. Kishida, K., Yamauchi, Y. & Guzik, A. Study of optical fibers strain-temperature sensitivities using hybrid Brillouin-Rayleigh System. *Photonic Sensors* **4,** 1–11 (2014).

30. Kogure, T. *et al.* Fiber optic strain measurements using distributed sensor system under static pressure conditions. *BUTSURI-TANSA(Geophysical Explor.* **68,** 23–38 (2015).

31. Xue, Z. *et al.* Effects of hydrostatic pressure on strain measurement with distributed optical fiber sensing system. *Energy Procedia* **63,** 4003–4009 (2014).

32. Xue, Z. & Hashimoto, T. Geomechanical Monitoring of Caprock and Wellbore Integrity Using Fiber Optic Cable: Strain Measurement from the Fluid Injection and Extraction Field Tests. *Energy Procedia* **114,** 3305–3311 (2017).

33. Vermorel, R. & Pijaudier-Cabot, G. Enhanced continuum poromechanics to account for adsorption induced swelling of saturated isotropic microporous materials. *Eur. J. Mech. A/Solids* **44,** 148–156 (2014).

34. Levine, J. R. Model study of the influence of matrix shrinkage on absolute permeability of coal bed reservoirs. *Geol. Soc. London, Spec. Publ.* **109,** 197–212 (1996).

35. Lie, K.-A. An introduction to reservoir simulation using MATLAB: user guide for the Matlab Reservoir Simulation Toolbox (MRST). SINTEF ICT. (2014).

36. Krause, M., Krevor, S. & Benson, S. M. A procedure for the accurate determination of sub-core scale permeability distributions with error quantification. *Transp. porous media* **98,** 565–588 (2013).